Reactive and Functional Polymers 200 (2024) 105923

Contents lists available at ScienceDirect

Reactive and Functional Polymers

journal homepage: www.elsevier.com/locate/react

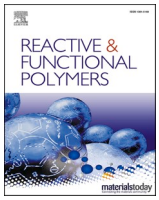

Anatase and rutile nanoparticles in photopolymer 3D-printed nanocomposites: Band gap-controlled electron interactions in free-radical and cationic photocuring

Martina Korčušková [a], Juraj Svatík [a], Wiktoria Tomal [b,c], Aneta Šikyňová [d], Vishakha Vishakha [a], Filip Petko [b,e], Mariusz Galek [e], Paweł Stalmach [b], Joanna Ortyl [b,e], Petr Lepcio [a,*]

[a] Central European Institute of Technology, Brno University of Technology, Purkyňova 123a, 612 00 Brno, Czech Republic
[b] Cracow University of Technology, Faculty of Chemical Engineering and Technology, Warszawska 24, 31 155 Cracow, Poland
[c] Polish Academy of Sciences, Jerzy Haber Institute of Catalysis and Surface Chemistry, Niezapominajek 8, 30-239 Cracow, Poland
[d] Institute of Biostatistics and Analyses, Faculty of Medicine, Masaryk University, Kamenice 126/3, 625 00 Brno, Czech Republic
[e] Photo Hitech Ltd., Life Scieence Park, Bobrzynskiego 14, 30-348 Cracow, Poland

ARTICLE INFO

Keywords:
Photoinitiation
Titanium dioxide
electron transfer
Cyclic voltammetry
Conversion

ABSTRACT

The preparation of functional photopolymer nanocomposites is affected by both the physical and chemical interactions of nanoparticles (NPs) and polymer resin. Some NPs, such as semiconducting metal oxides, may contribute by their photocatalytic behavior and electron transfer, influencing the kinetics of the photopolymerization reaction. This study has investigated the complex effect of titanium dioxide (TiO_2) NPs in anatase and rutile form on the conversion, kinetics, and printability of free-radical and cationic photopolymerization resin. Two different polymorphs of TiO_2 NPs ensured identical chemical properties, but different physical effects related to their varying band gap energies and electron transfer efficiency. These parameters were found to be crucial for influencing the photopolymerization kinetics. While rutile showed a more pronounced enhancement of the free-radical photopolymerization's conversion and kinetics, cationic photopolymerization was favourably affected only by anatase NPs due to the photosensitization effect. These findings are critical in understanding and designing functional nanocomposite materials processed by vat photopolymerization 3D printing that could find use in optical, medical, or environmental applications.

1. Introduction

Vat photopolymerization 3D printing is an additive manufacturing technique known for its accessibility, highest resolution, and smoothest surface among the affordable 3D printers. On the other hand, this method offers only a limited number of photopolymerizable materials compatible with the common 3D printers [1]. The most frequently used commercial resins are based on acrylates and methacrylates, cured through the free-radical mechanism, followed by cationically polymerized epoxy resins [2]. The free-radical mechanism is favored for the fast propagation, allowing high printing speeds, and termination, which prevents overpolymerization and improves the print's dimensional accuracy. On the other hand, the advantages of cationic photoinitiation are insensitivity to oxygen inhibition, minimal sensitivity to water, lower shrinkage, and the possibility of dark curing, i.e., reacting even after light exposure ceased [3–6]. The lack of material variability could be partially substituted by adding nanofillers due to their impact on mechanical, thermal, optical, and functional properties [7–9]. The most commonly used nanofillers in vat 3D printing are carbon nanoparticles (NPs) [10–13], metal NPs [14,15], and metal oxide NPs [7,16–19].

Certain photoactive NPs, including semiconducting metal oxides, such as ZnO, TiO_2, or Fe_2O_3, have been reported to act as free-radical photoinitiators and photosensitizers. The photocatalytic ability of NPs depends on their band gap energy, which must be equal to or smaller than the energy of the curing light to generate charge carriers [20–23]. Upon illumination with light of suitable energy, these semiconducting NPs generate free electrons (e^-) in the conduction band and free holes (h^+) in the valence band, which are subsequently transferred to the NP surface and initiate curing (Fig. S1). Photocatalytic NPs can potentially replace harmful substances used as commercial photoinitiators [24,25].

* Corresponding author.
E-mail address: petr.lepcio@ceitec.vutbr.cz (P. Lepcio).

https://doi.org/10.1016/j.reactfunctpolym.2024.105923
Received 19 January 2024; Received in revised form 25 April 2024; Accepted 30 April 2024
Available online 1 May 2024

During the free-radical photoinitiation (Fig. S2), the photoinitiator, such as the phenylbis(2,4,6-trimethylbenzoyl)phosphine oxide (BAPO), is illuminated with light, leading to the singlet excited state (^{1}PI), triplet excited state (3PI), and subsequently, photofragmentation. That generates a radical pair through α-cleavage process. These radicals react with monomer molecules in the propagation step [26]. Moreover, BAPO can act as both an electron acceptor and a donor, and it can undergo oxidation (of the phenolic group) or reduction (of the carbonate group). Free electrons generated in NPs can also react with BAPO and form an excited radical state by electron transfer and subsequent photoinitiator reduction. Thus, NPs can represent an effective method for free-radical photosensitizing.

The most widely used cationic photoinitiators are diaryliodonium salts, also known as ionium salts (IS). Upon light illumination (Fig. S2), they create an excited singlet state, which undergoes photodissociation via the homolytic or heterolytic mechanism of the low-energy carbon-iodine bond. Typically, the homolytic mechanism prevails, generating highly reactive aryl radicals and aryl iodonium radical cations coordinated with the original salt's anion as a counterion. The radical cation can detach hydrogen from the surrounding monomer and form protonic acid, whose strength depends on the type of its anion. It could also be generated by heterolytic dissociation. The propagation of photopolymerization then begins with protonic acid reacting with monomers through ring-opening polymerization in the case of epoxy monomers [27]. For a cationic mechanism, NPs can act as photosensitizers and absorb light to form excited species, subsequently creating an excited complex between diaryliodonium salt and NPs. The onium salt is then reduced by the electron transfer, and the unstable intermediate is rapidly decomposed, preventing the electron back-transfer. Moreover, photosensitizers can also facilitate the reaction and increase the reaction yield by extending the wavelength range of effective light absorption [28].

For commercial vat photopolymerization 3D printers using stereolithography (SLA) or digital light processing (DLP) technology, titania (TiO_2) represents an ideal semiconducting nanofiller with photocatalytic properties. Titania is known to be an excellent photoactive compound with a band gap energy of ~3–3.2 eV, depending on its polymorph. Moreover, it is a nontoxic, biocompatible, and chemically stable compound with outstanding mechanical, optical, and physical properties. In nature, titania occurs at ambient pressure in three natural crystalline modifications: anatase, rutile, and brookite [16,29,30]. Anatase and rutile polymorphs have been extensively studied for their environmental application as photocatalysts in organic pollutant degradation. Rutile represents the most stable phase, while anatase is metastable and can be transferred to rutile after heating [31]. They both have tetragonal crystal lattices characterized by $I4_1/amd$ and $P4_2/mnm$ space groups for anatase and rutile, respectively.

Charge carriers generated upon light illumination produce reactive oxygen species (ROS) at the surface of TiO_2 NPs. The surface chemical reactions of free electrons and holes produce hydroxyl radicals and superoxide radical anions, which form hydrogen peroxide. These ROS are further involved in the photodegradation process of environmental contaminants [30,32,33]. The same mechanism based on the photoactivity of TiO_2 can be used in vat 3D printing, where the generated charge carriers interact with the polymer resin molecules.

TiO_2 NPs were previously investigated to improve the mechanical and thermal properties of 3D-printed nanocomposites [16,34]. In addition, titania nanocomposites showed a higher photocatalytic efficiency in environmental applications than bare individual NPs due to the reduced rate of charge carrier recombination caused by better charge separation on the photocatalyst surface [35–37]. As photopolymerization reactions are carried out under mild conditions, vat 3D printing with TiO_2 can lead to various applications in biomedicine, dentistry, sensor production, or wastewater treatment [38,39]. Other advanced applications can be achieved by modifying TiO_2 NPs with dopants [40,41] or surface functionalization [42].

Nevertheless, the growing demand for these materials requires further study of the photopolymerization kinetics. NPs interact chemically with the reaction by interacting with the surrounding polymer chains at the NP surface and physically through light scattering or absorption and the nanoreinforcement effect [7,43]. All these effects, including NP photoactivity, alter the photopolymerization kinetics, resulting in different conversion degrees – a critical factor determining the nanocomposites' thermomechanical and functional properties [13,16]. Although several studies have already addressed the vat 3D printing process using TiO_2 NPs, their effect on the reaction mechanism, particularly cationic photoinitiation, has not been sufficiently described.

Herein, TiO_2 NPs in two forms (anatase and rutile) were used to determine their impact on photopolymerization kinetics using free-radical and cationic types of representative 3D printing curable resins. Anatase and rutile have identical chemical compositions but exhibit different band gap energies, enabling us to understand better the physical effects of nanocomposite photopolymerization. The course of the photopolymerization reaction was related to different processing parameters, e.g., curing light wavelength and intensity, curing time, or NP concentration. The photopolymerization kinetics was monitored by real-time FTIR and photo-DSC analyses, while the printability was studied using Jacobs working curves. In addition, the distribution of NPs within the polymer matrix was monitored, as it is a vital processing parameter to obtain uniform properties in the entire nanocomposite volume.

2. Experimental

2.1. Materials

A UV photosensitive radical resin was mixed from a urethane acrylate oligomer (CN966H90) and two acrylic monomers (SR900, SR833S) obtained from Arkema (France) in the weight ratio 4: 3: 3 with an addition of 4% of phenylbis (2,4,6-trimethylbenzoyl)-phosphine oxide (BAPO) as a type I photoinitiator. Cationic resin was mixed from 3,4-epoxycyclohexylmethyl 3,4-epoxycyclohexanecarboxylate (ECC) and neopentyl glycol diglycidyl ether (NGDE), both purchased from Sigma-Aldrich (Germany), in the weight ratio of 7: 3. The cationic photoinitiator (7-(2-cyano-2-phenylvinyl)-2,3-dihydrothieno[3,4-b][1,4] dioxin-5-yl)(phenyl)iodonium hexafluorostibate(V) synthesized at the Photo Hitech Ltd. was used at 1% *w*/w [44]. The anatase (10–25 nm) and rutile (30 nm) polymorphs of titanium dioxide (TiO_2) NPs were obtained from Nanoshell (UK) and used as received.

2.2. 3D printing and curing

The nanocomposite formulations were mixed with a magnetic stirrer and sonicated with an ultrasonic tip (Bandelin Sonopuls, Germany) to secure a good NP dispersion. The samples based on free-radical resin were 3D printed with the Original Prusa SL1S printer (Prusa, Czech Republic), which is a VPP-LED 3D printer using masked stereolithography (M-SLA) technology, equipped with a 405 nm UV LED source (2.07 mW·cm^{-2}). All free-radical samples for STEM observation were 3D printed with first layer exposure of 20 s, while exposure of all other layers was 8 s, and subjected to further analysis with post-curing at 40 °C for 10 min using the Original Prusa CW1 curing and washing unit (Prusa, Czech Republic) with an irradiation intensity of 10 mW·cm^{-2}. The cationic resin-based samples were 3D printed with the Nobel 1.0 A (XYZprinting, Taiwan) VPP 3D printer using 405 nm laser stereolithography (SLA) technology with a maximum light intensity of 15.67 mW·cm^{-2}.

2.3. Optical and electrochemical properties

Raman measurement was carried out using the Confocal Raman imaging system Alpha 300 R (Witec, Germany) with a green 532 nm

laser, 15 mW laser power, 600 g·cm^{-1} grating, and an optical microscope with a 10× magnification lens. The integration time was set to 1 s and the number of accumulations to 20.

Diffusion reflectance spectroscopy (DRS) was performed using a V-770 double-beam UV/Vis/NIR spectrophotometer (Jasco, Japan). The powdered NPs were measured with the aid of the integrating sphere ISN-923 to obtain absorbance and diffuse reflectance simultaneously. The band gap was established by the tools in the OEM software according to the Tauc plot:

$$\alpha h\upsilon = A\left(h\upsilon - E_g\right)^n \quad (1)$$

where α is the absorption coefficient, h is Planck constant, υ is the frequency of photons, A is the proportional constant, E_g is the band gap energy, and n is a constant dependent on the sample transition equal to 0.5 or 2 for the direct and indirect allowed transitions, respectively. The measured reflectance spectra were transformed into the absorption spectra by the Kubelka-Munk function [45].

Photolysis was measured under exposure to VIS-LED-405 led light (M405L2) powered by a DC2200 regulated power supply (both Thorlabs Inc., USA). 1 mg of NPs dispersed in 25 mL of acetonitrile were sonicated (Bandelin Sonopuls, Germany) and then photolyzed in a quartz cuvette for 20 min with a forward current of the 405 nm LED set to 100 mA. UV-VIS spectra were recorded using a weak broadband beam from a UV/VIS deuterium-halogen light source (SL5, StellarNet USA).

Electrochemical properties were determined by cyclic voltammetry (CV). Measurements were carried out with an electrochemical analyzer M161 and an electrode support M164 (from MTM-ANKO, Cracow, Poland). The experiments were carried out in a three-electrode configuration with a platinum-core electrode with a diameter of 1 mm as the working electrode, a silver chloride electrode as the reference electrode, and a supporting platinum electrode in the form of a wire with a diameter of 0.7 mm. A 0.1 M solution of tetrabutylammonium hexafluorophosphate (from Sigma Aldrich) in acetonitrile was used as the base electrolyte. The tests were conducted for solutions of the test compounds in acetonitrile, which were previously degassed using argon. The scanning rate of the sample was 0.1 V/s, and ferrocene was used as a standard. The CV experiments were conducted in triplicate and the experimentally determined measurement error is 1.53 mV.

2.4. Assessment of photopolymerization kinetics and printability

Photopolymerization kinetics was monitored by real-time FTIR spectroscopy with an FT/IR-6700 spectrometer (Jasco, Japan). The sample was cured using two different light sources: 365 nm M365L3 and 405 nm M405L4 VIS-LED diodes regulated by a DC2200 power supply (all Thorlabs Inc., USA). The intensity of the emitted light was controlled by the forward current. The radical resin was cured using 365 and 405 nm LEDs at two different levels of light irradiance (1.15 mW·cm^{-2} and 1.75 mW·cm^{-2}) corresponding to the current of 2.5 mA and 10 mA.

The cationic resin was cured only with the 405 nm at 4.87 mW·cm^{-2} (≈ 100 mA). A small amount of sample was placed between two polypropylene films to reduce the oxygen inhibition (for the free-radical mechanism) or onto a barium fluoride pellet (for the cationic composition). The change in FTIR absorbance peaks was continually measured for 200–800 s while the samples were irradiated by the LED. The curing of the free-radical resin was evaluated from the C=C acrylic double bond signal between 1610 and 1640 cm^{-1}. The cationic resin was tracked by the 760–830 cm^{-1} and 850–950 cm^{-1} peaks corresponding to the ECC and NGDE vibrations, respectively. The conversion X was calculated from the decreasing peak area according to the formula:

$$X(\%) = \left(1 - \frac{A_{after}}{A_{before}}\right) \bullet 100 \quad (2)$$

where A_{before} and A_{after} represent the peak area before and after the polymerization. We note that the standard deviation of the final conversion is very small, at 0.75 pp.

Photo-DSC measurements were performed using Discovery DSC (TA Instruments, USA) under isothermal conditions at 25 °C. A small amount of samples (15 μL) in uncovered aluminium pans was illuminated by continuous non-pulsing 405 nm M405L4 VIS-LED diode (Thorlabs Inc., USA) with a light irradiance of 2.07 mW·cm^{-2} for free-radical samples and 15.67 mW·cm^{-2} for cationic samples. The light irradiance was chosen close to the illumination capabilities of the respective 3D printers used in this study. The first 60 s of the measurement were used to collect a stable baseline in dark conditions. The illumination onset, marking the start of the photocuring, was set to $t = 0$ min. The heat flow rate dQ/dt was calculated as the first derivative of the heat flow using the in-built functions of the TRIOS OEM software.

Jacobs working curves express the printability of the material. They comprise a logarithmic linear plot of cure depth (C_d) and the curing energy (E_0), which is determined by the irradiation intensity and curing time. The critical energy (E_c) required to initiate the photopolymerization of a solid layer is calculated as the intersection of the Jacobs working curve with the x-axis. The slope of the Jacobs working curve defines the penetration depth (D_p), at which the penetrating light intensity falls to e^{-1} of the surface intensity. The light penetration through the resin follows the Beer-Lambert relationship, and the basic Jacobs curve equation is expressed as:

$$C_d = D_p \bullet ln\left[\frac{E_0}{E_c}\right] \quad (3)$$

To construct the Jacobs working curves, square geometries (10 × 10) mm^2 were printed with curing times varying between 10 and 60 s and 120–480 s for the free-radical and cationic samples, respectively.

2.5. Structural analysis

Scanning transmission electron microscopy (STEM) observations were performed on 70 nm ultramicrotome cuts with a Mira 3 XMU microscope (Tescan, Czech Republic) in a bright field at 30 kV acceleration voltage. The Ultrasmall-angle X-ray scattering (USAXS) samples were 3D printed in the dimensions of (25 × 25) mm^2 square with a 1 mm thickness and measured with a SmartLab 9 kW X-ray diffractometer (Rigaku, Japan) at 45 kV and 150 mA. The 2θ values ranged between 0.05 and 0.5°, and the step degree was 0.0010. The time duration for each sample measurement was 22 min. Nano solver software was used to find the nanoparticle distribution by removing the background using the reference measurement using an unfilled reference sample followed by slit information(Ge220), scale factor (0.0001), particle pore size analysis, and particle size distribution. Notably, the average diameter relates to the size of aggregates/clusters rather than individual NPs.

3. Results and discussion

3.1. Optical characterization

Firstly, the purity of TiO_2 NPs was verified by Raman spectroscopy [30]. Anatase exhibits active Raman vibrations with the absorption maxima at 143.1 cm^{-1} (E_g(1)), 195.3 cm^{-1} (E_g(2)), 395.4 cm^{-1} (B_{1g}(1)), 515.9 cm^{-1} (B_{1g}(2) + A_{1g}) and 637.4 cm^{-1} (E_g(3)). On the other hand, rutile exhibits active Raman vibrations with maxima at 143.1 cm^{-1} (B_{1g}), 446.0 cm^{-1} (E_g), and 610.0 cm^{-1} (A_{1g}). On top of that, rutile shows a characteristic strong second-order Raman scattering with a maximum at 238.6 cm^{-1} [46,47]. These characteristic vibrational frequencies confirmed the presence of pure anatase and rutile polymorphs in the NPs (Fig. S3).

Secondly, the optical properties of pure TiO_2 NPs were assessed by determining the band gap energy and optical stability. Therefore, anatase and rutile were subjected to DRS and photolysis [43]. The

absorbance spectra and the Tauc plot with a graphically indicated E_g determination are shown in Fig. S4. TiO_2 is an indirect band gap semiconductor, giving the $n = 0.5$. The detected E_g was 3.16 eV and 2.97 eV for anatase and rutile, respectively. That corresponds to wavelengths of 392 nm and 417 nm, respectively. Therefore, the 405 nm light used for curing has an energy above the rutile's band gap but below that of the anatase.

The rutile and anatase photostability was investigated on NPs dispersed in acetonitrile under irradiation with 405 nm light (Fig. 1). In both cases, the NPs absorbance continuously decreased with the illumination time, indicating either an interaction between the NPs and the incident photons or sedimentation. While the anatase's absorption intensity decreased in time, probably due to the sedimentation, rutile showed increasing absorption but also qualitative changes in the spectrum's shape (Fig. 1). That manifests physicochemical changes on the rutile's surface through the creation of free electrons and holes as photoproducts.

3.2. Electrochemical characterization

Cyclic voltammetry (CV) is an electrochemical technique studying molecular species' reduction and oxidation processes. This technique can also be employed in investigating electron transfer-initiated chemical reactions, such as catalysis [48]. As described above, BAPO can undergo both oxidation and reduction, which can be detected as peaks in cyclic voltammograms (Fig. 2). On the other hand, TiO_2 NPs can generate charge carriers only under light illumination with sufficient energy, and they showed no significant electron-transfer processes during CV measurement under dark conditions (Fig. S5).

Nevertheless, TiO_2 NPs were found to act as sensitizers when tested in connection with the BAPO free-radical photoinitiator. As both oxidation and reduction of BAPO photoinitiator are possible, CV measurement was performed in two separate cycles to evaluate these individual processes, each consisting of two consecutive scans (oxidation/reduction or reduction/oxidation). In the reduction cycle, BAPO exhibited a reduction peak during the reductional scan coupled to an opposite reverse peak during the oxidational scan (Fig. 2A). These peaks are characterized by the peak potentials (E_{p1} and $E_{p2,}$ respectively) and the half-wave potential of the redox reaction ($E_{1/2}$), describing the potential at which half of the oxidation or reduction took place during the CV experiment (Table 1). The peak currents (i_{p1}, i_{p2}) determine the reversibility of the process (Table 1). In general, as the difference between E_{p1} and E_{p2} is always $>59.2/n$ mV, where n is a number of transferred electrons, all redox reactions taking place through the reduction are quasi-reversible. The degree of reversibility could be predicted from the i_{p1}/i_{p2} value. The closer it is to 1, the more reversible the reaction is [49]. The example of evaluating the mentioned characteristics is shown in Fig. S6, and the determined values are presented in Table 1. The CV analysis clearly showed that rutile NPs had a more significant impact on BAPO oxidation while having a lesser negative effect on the BAPO reduction than anatase. Therefore, rutile is anticipated to yield better photosensitizing properties of the BAPO free-radical photoinitiator compared to anatase, as will be verified later.

Comparing the $E_{1/2}$ values for the reduction process of pure BAPO and BAPO with anatase or rutile, all reductional processes remain quasi-reversible. However, both BAPO/NPs mixtures exhibit less negative values, indicating a shift in the thermodynamics of an electron-transfer to an energetically less favorable redox reaction. That is further supported by the peak potentials (E_{p1}, E_{p2}), where the reduction peaks (E_{p1}) are shifted to less negative values while the reverse oxidation peaks (E_{p2}) are shifted to more negative values (Table 1). This shift was more pronounced for anatase compared to rutile. Additionally, anatase NPs significantly increase the i_{p1}/i_{p2} ratio, indicating that the reaction is less reversible than for pure BAPO.

The second cycle determined only a single oxidation peak in the oxidational scan (Fig. 2B). The absence of a reverse peak during the consecutive reductional scan indicates the reaction's irreversibility, concluding that the redox reactions at the electrodes occur in a non-equilibrium state. Irreversible reactions can be characterized only by the peak potential (E_{p1}). Anatase and rutile NPs lowered the E_{p1} values, indicating that the NPs move the reaction to lower potentials due to enhanced reaction kinetics or reaction rate. The CV analysis clearly showed that rutile NPs had a more significant impact on BAPO oxidation while having a lesser negative effect on the BAPO reduction than anatase. Therefore, rutile is anticipated to yield better photosensitizing properties of the BAPO free-radical photoinitiator compared to anatase, as will be verified later.

TiO_2 NPs can also act as a photosensitizer of ionium salt (IS) in cationic photopolymerization. In general, IS acts as an electron acceptor, whereas NPs represent electron donors in the system. That infers a preferential oxidation process in the system. Nevertheless, IS reduction (Fig. 3A) could also be carried out at appropriate potential where NPs act as electron acceptors. A sole peak in the reductional scan assumes an irreversible reaction. Nevertheless, a shift to lower values of peak potentials (Table 2) can be observed after the NP addition, which means that both types of TiO_2 NPs favourably influence the reaction.

On the other hand, the IS oxidation is quasi-reversible (Fig. 3B), due to the second reversible peak in the reductive scan, even though the peak

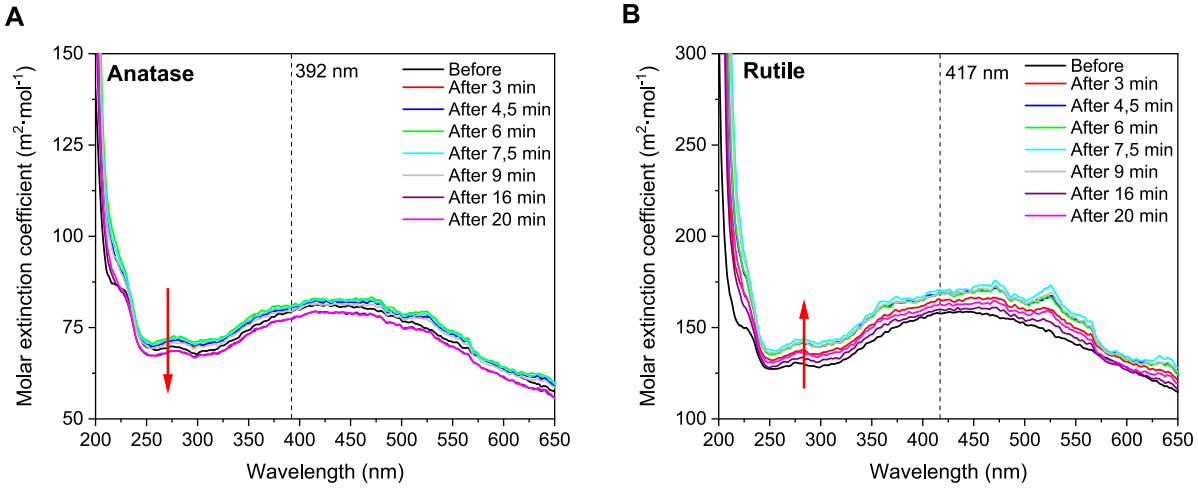

Fig. 1. Photolysis of anatase and rutile nanoparticles dispersed in acetonitrile shows a decay of absorption intensity caused by illumination with 405 nm light. The band gap energies of anatase and rutile NPs correspond to 392 nm and 417 nm, respectively (Fig. S4).

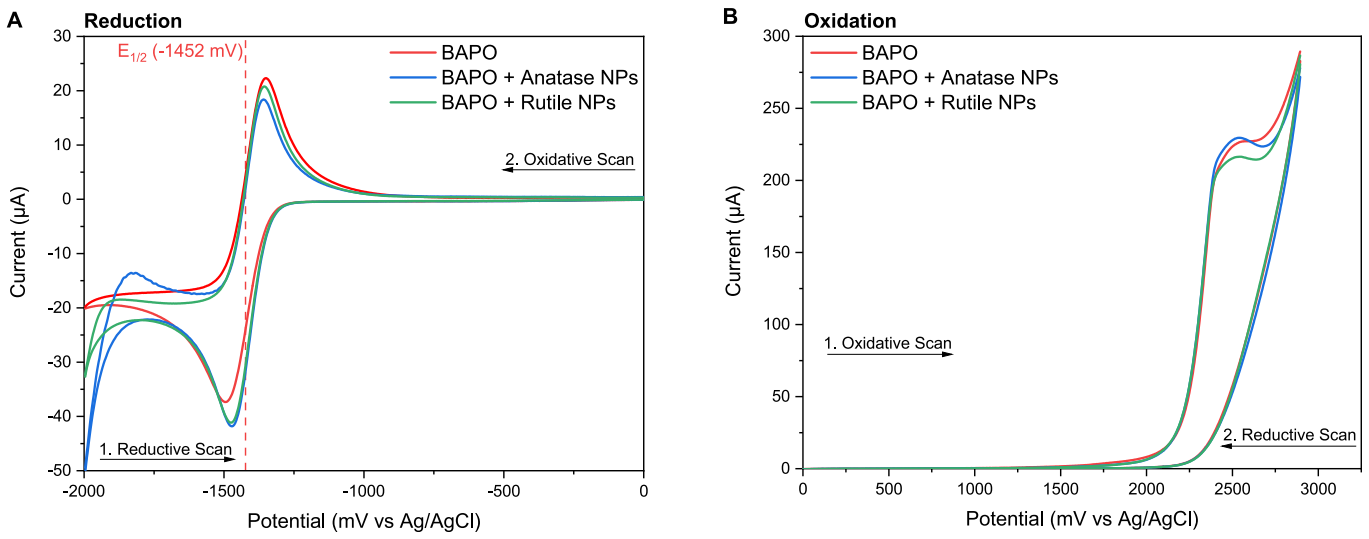

Fig. 2. Reduction (A) and oxidation (B) of pure BAPO and mixture of BAPO with anatase and rutile nanoparticles measured by cyclic voltammetry using acetonitrile as a solvent, 0.1 M solution of tetrabutylammonium hexafluorophosphate as the base electrolyte, 1 mm platinum-core working electrode, Ag/AgCl reference electrode, and 0.7 mm supporting platinum electrode at a scan rate of 0.1 V/s. The experimentally determined measurement error is 1.53 mV.

Table 1
Values of half-wave potential of redox reaction ($E_{1/2}$), peak potentials (E_{p1}, E_{p2}) and ratio of peak currents (i_{p1}/i_{p2}) for reduction and oxidation processes of the free-radical photoinitiator obtained from cyclic voltammetry. The experimentally determined measurement error is 1.53 mV.

	Reduction				Oxidation
Sample	$E_{1/2}$ (mV)	E_{p1} (mV)	E_{p2} (mV)	i_{p1}/i_{p2}	E_{p1} (mV)
BAPO	−1423	−1496	−1350	0.96	2567
BAPO + Anatase NPs	−1415	−1472	−1358	1.15	2543
BAPO + Rutile NPs	−1416	−1476	−1356	1.02	2537

currents ratio (i_{p1}/i_{p2}) is far from 1. However, anatase and rutile NPs antagonistically affect the reaction course. Anatase increases the measured current, lowers the $E_{1/2}$, E_{p1} and E_{p2} potentials and also decreases i_{p1}/i_{p2}, improving the process' reversibility. Therefore, anatase NPs improve the electron-transfer thermodynamics by increasing the kinetics or reaction rate, implying photosensitizing ability in conjunction with the cationic photoinitiator. On the contrary, rutile NPs shift these properties in opposite directions to higher values, indicating an adverse effect on the electron-transfer efficiency.

Table 2
Values of the half-wave potential of redox reaction ($E_{1/2}$), peak potentials (E_{p1}, E_{p2}) and the ratio of peak currents (i_{p1}/i_{p2}) for reduction and oxidation processes of the iodonium salt photoinitiator obtained from cyclic voltammetry. The experimentally determined measurement error is 1.53 mV.

	Reduction	Oxidation			
Sample	E_{p1} (mV)	$E_{1/2}$ (mV)	E_{p1} (mV)	E_{p2} (mV)	i_{p1}/i_{p2}
IS	−311	1891	1840	1942	2.85
IS + Anatase	−388	1884	1832	1935	2.26
IS + Rutile	−388	1899	1844	1953	2.88

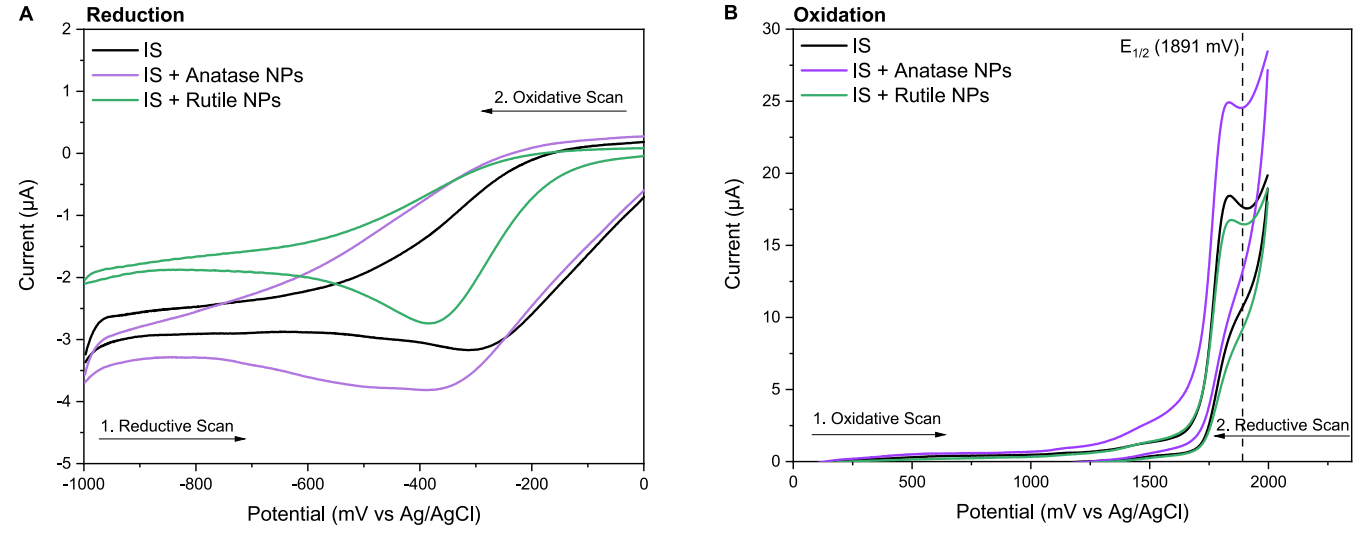

Fig. 3. Reduction (A) and oxidation (B) of pure ionium salt (IS) and a mixture of IS with anatase and rutile nanoparticles measured by cyclic voltammetry using acetonitrile as a solvent, 0.1 M solution of tetrabutylammonium hexafluorophosphate as the base electrolyte, 1 mm platinum-core working electrode, Ag/AgCl reference electrode, and 0.7 mm supporting platinum electrode at a scan rate of 0.1 V/s. The experimentally determined measurement error is 1.53 mV.

3.3. Nanoparticle dispersion

Particle spatial distribution is an essential factor determining the intensity of interfacial interactions near the NP surface. Due to attractive Van der Waals forces, NPs tend to aggregate or agglomerate into clusters, reducing the effective surface area exposed to monomer/polymer [50]. On the other hand, a uniform NP dispersion results in a larger surface area and lowers the heterogeneity throughout the body volume due to the better distribution of the nanoreinforcement effect. NP dispersion was characterized on 3D-printed free-radical acrylic composites by USAXS analysis and STEM observations. The average diameter determined by USAXS (Table 3) is approximately 6–15 times larger than the size of individual particles, suggesting the presence of clusters. [8] Therefore, slightly weakened interfacial effects could be expected in the system compared to the individually dispersed particles. Rutile (~200–230 nm) and anatase (~150 nm) clusters scale in almost the same ratio as the NP size (30 nm and 10–25 nm, respectively). The differences may be caused by variance in surface energy and space groups of the two TiO_2 polymorphs.

This finding correlates with the cluster density, represented by number of NP clusters per mm^2 of the 70 nm thick ultramicrotome cut observed by STEM (Fig. S7–8), which showed nearly linear dependence on the NP concentration (Fig. 4). Anatase formed more clusters than rutile at almost all tested concentrations because of its smaller particle and cluster size. The deviation at small concentrations was considered insignificant and attributed to experimental error because STEM provides only local information from areas of typically tens to hundreds of microns. Therefore, the number of clusters is more susceptible to experimental error than the size obtained from SAXS, especially at the low-concentration boundaries. Moreover, the number of clusters is estimated from a 2D projection in ultramicrotome cuts, which are only 70 nm, approx. 2–3 times thinner than the cluster size, distorting the probability distribution function. Finally, SAXS supposedly overestimates the cluster size due to incorporating polymer chains trapped between the particles inside the cluster into the overall size of the inclusions. Nevertheless, we conclude that the same dispersion quality was maintained within the tested concentration range, so the dispersion-related effects, such as varying curing efficiency [13] or mechanical properties [9], could be neglected in our conclusions.

3.4. Free-radical photopolymerization

Photopolymerization is generally a first-order reaction consisting of photodecomposition, initiation, propagation, chain transfer, and termination. The kinetics of all reaction steps is affected by the composition of the system, the amount and activity of the photoinitiator, the presence of the photosensitizer, oxygen inhibition, temperature, and other complex factors [51]. The effect of TiO_2 NPs on the kinetics of the free-radical acrylic resin was monitored in the range between 0.05 and 5 wt% of NPs by real-time FTIR, photo-DSC, and Jacobs working curves. The real-time FTIR revealed the dependence of acrylic double bond conversion X on the reaction time. The photopolymerization kinetics curve is characterized by a slope expressing the conversion rate dX/dt and the final conversion (Fig. 5) [48]. The band gap energies of anatase and rutile NPs correspond to 392 nm and 417 nm, respectively (Fig. S4). Therefore, the real-time FTIR was performed at 365 (Fig. S9A) and 405 nm (Fig. S10A) light exposure to investigate the role of the band gap on the photocuring.

Table 3
Average cluster diameter of nanoparticle clusters fitted from the USAXS data.

Nanoparticle concentration (wt%)	Average cluster diameter (nm)	
	Anatase	Rutile
0.05	149.1	240.9
0.1	151.6	204.0
0.5	151.5	228.6
1	155.5	201.8

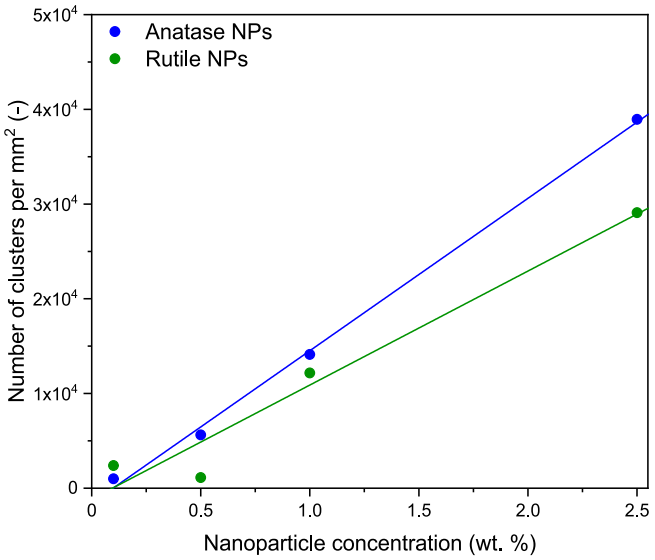

Fig. 4. Number of nanoparticle clusters per 1 mm^2 of the 70 nm thick ultramicrotome cut observed by STEM as a function of nanoparticle concentration. The lines represent linear fits of the experimental data.

Using a 405 nm LED light (Fig. 5A, B), both anatase and rutile NPs showed higher final conversions than the unfilled radical resin (80.6%) at all investigated NP concentrations. Nevertheless, higher conversion rates were observed for rutile (up to 88%), correlating well with the CV results (Fig. 2). Since the photon energy (3.06 eV) exceeds the rutile's E_g (2.97 eV), the incident photons can excite charge carriers within NP. These subsequently enter the reaction as a photoinitiator or photosensitizer. On the other hand, the E_g of anatase (3.16 eV) is higher than the photon energy, which prevents the formation of free charge carriers. However, UV LED light sources, including that in the SL1S 3D printer, produce a narrow distribution spectrum around the maximum wavelength rather than a strictly monodisperse light [52]. Therefore, a small portion of the emitted photons exceeds in energy also the anatase's E_g, granting the anatase some photoactivity at these conditions and increasing the final conversion. The same trend can be seen in Fig. 5B, where both anatase and rutile increase the dX/dt, while rutile has a more pronounced effect.

The final conversion of pure unfilled resin is higher at 365 nm than at 405 nm (Fig. 5C, D) because of the higher BAPO's absorbance at lower wavelengths (Fig. S14). The NP effect is marginal at low concentrations ($\leq$ 1 wt%). However, higher NP content deteriorates the final conversion (Fig. 5C) and dX/dt (Fig. 5D), which may signify the predominance of competing reactions (e.g., recombination, thermalization or trapping). Moreover, rutile has a more pronounced adverse effect than anatase. That indicates not only the light energy (3.40 eV for 365 nm) and E_g being important factors, but also the absorption efficiency and efficiency of electron transfer influence the course and kinetics of the photocatalytic reaction. The more emitted photons able to generate an electron-hole pair there are, the higher electron transfer efficiency is observed in the semiconductor. Moreover, anatase NPs generally exhibit a lower recombination rate [36], causing a higher photocatalytic efficiency at 365 nm.

The findings described above were also verified using a higher light intensity (1.75 $mW \cdot cm^{-2}$, Fig. S12–13) and thus a higher number of emitted photons available for the photoinitiation. The final conversion and dX/dt were higher for both 405 and 365 nm compared to lower intensity (1.15 $mW \cdot cm^{-2}$), reaching around 90%. At 405 nm (Fig. S13A, B), rutile showed higher conversion and faster kinetics than anatase, yet the difference was less prominent than at low intensity exposure and

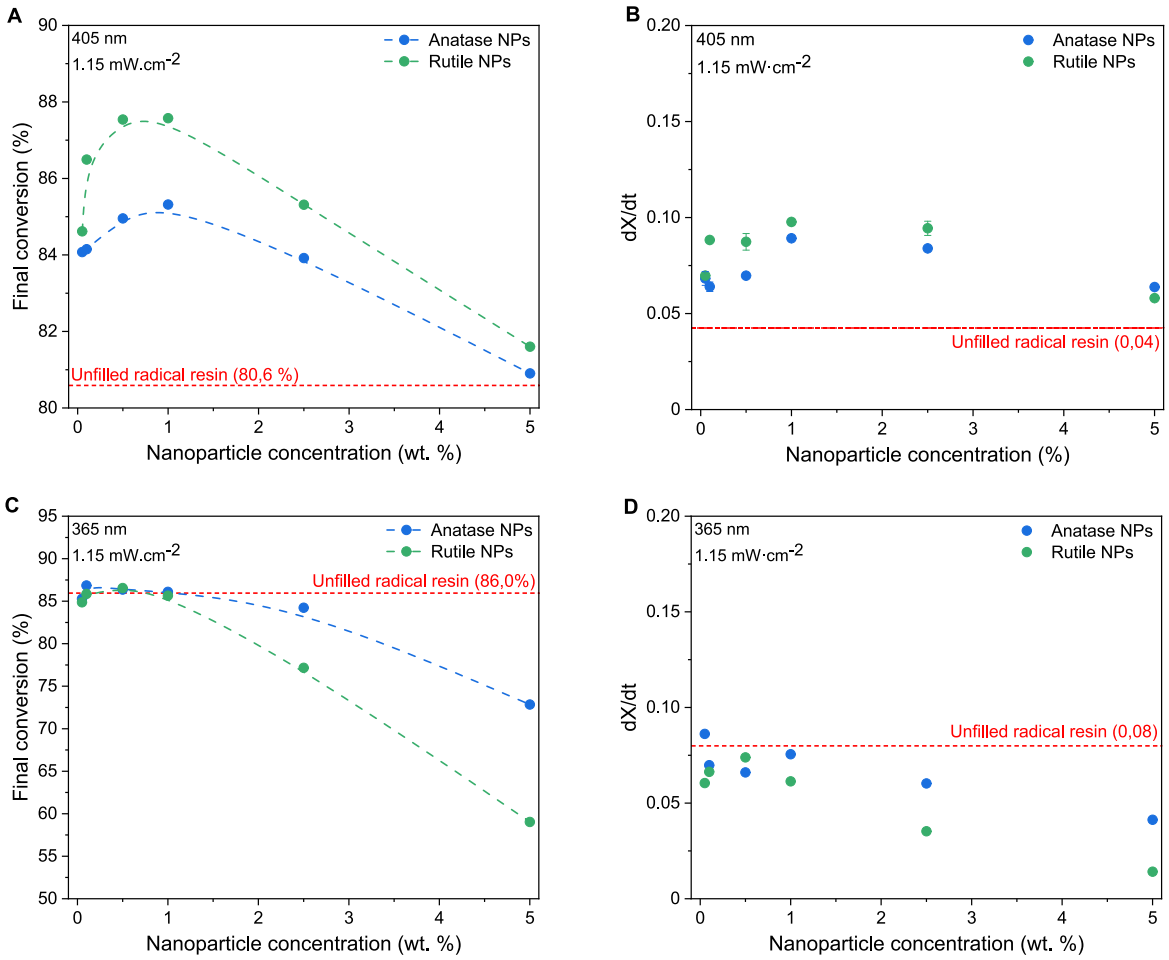

Fig. 5. Final conversion of double acrylic bonds of the radical resin and the conversion rate (dX/dt) as a function of the nanoparticle concentration, measured at 405 nm (A, B) or 365 nm (C, D) with light intensity of 1.15 mW·cm^{-2}. The dashed lines represent a guide for eyes. The standard deviation of final conversion (A, C) is very small, at 0.75 pp., and the error bars in (D) merges with the points.

their performance became comparable at higher NP concentrations. An unchanged trend with anatase providing higher reaction rates and final conversions was observed also at 365 nm (Fig. S13C, D).

Furthermore, the curing kinetics was monitored by photo-DSC analysis (Fig. 6A, B) [7]. As can be seen from the maximum of the exothermic peak (Fig. 6C), anatase NPs have slightly greater effect than rutile at low concentration ($\leq$ 0.5 wt%), but more prominent adverse effect at higher concentration. This may be caused by the proportion of electron-hole processes occurring inside the NPs after illumination. As we documented in our previous work [7], this technique measures the heat flow upon light exposure, which can be affected by additional enthalpic processes such as free-electron recombination, surface plasmon resonance of NPs, or the heterogenous character of the curing reaction. Besides participating in photopolymerization, free charge carriers undergo separation, thermalization, trapping, recombination, and final transport to the NP surface. During these processes, the energy of charge carriers can be released in the form of heat or light, which will affect the measured heat flow [53,54]. Thus, photo-DSC appears to be a less reliable technique compared to real-time FTIR. Nevertheless, the photo-DSC provides useful auxiliary information on the reaction course [50,51].

The heat flow rate dQ/dt (Fig. 6D) shows a similar dependence with an increasing trend up to approx. 1 wt% of NPs, followed by a decline at higher NP concentrations. Free charge carriers are formed on the NP surface at the beginning of the reaction due to the illumination. Subsequently, the photopolymerization is limited by either the above-mentioned reactions of charge carriers or the limited diffusion of monomers to the formed radicals. This behavior correlates with a decrease in reaction rate with increasing NP content due to a more pronounced diffusion limitation, and, potentially, particle aggregation.

Jacobs working curves (Fig. S15) revealed information about the printability of thin polymer layers during the 3D printing process. E_c and D_p as functions of the NP concentration are visualized in Fig. 7. Both types of NPs decreased the E_c (Fig. 7A) values except for small NP concentration ($\leq$ 0.1 wt%). This is in good correlation with real-time FTIR (Fig. 5) and photo-DSC analysis (Fig. 6), where a low NP content (0.05 wt%) caused no or only a slight increase in the measured values. The greatest effect on the photopolymerization reaction was observed by all three techniques between 0.1 and 1 wt% of NPs. Above this concentration, E_c varies only slightly. The same trend is also observed for D_p (Fig. 7B).

3.5. Cationic photopolymerization

Finally, the effect of TiO_2 NPs on the cationic photopolymerization was monitored analogically using real-time FTIR, photo-DSC, and Jacobs working curves. The light irradiance used for real-time FTIR measurement was 4.87 mW·cm^{-2} (405 and 365 nm), due to longer photoinduction times and overall slower reaction kinetics of the cationic photoinitiation mechanism. Conversion was deduced from two characteristic peaks – the epoxy group of ECC with a maximum at 790 cm^{-1} (Fig. S16) and the oxirane group of NGDE with a maximum at 910 cm^{-1} (Fig. S17). The final conversions and dX/dt of the ECC epoxy and NGDE oxirane groups after 800 s curing at 405 nm are shown as functions of

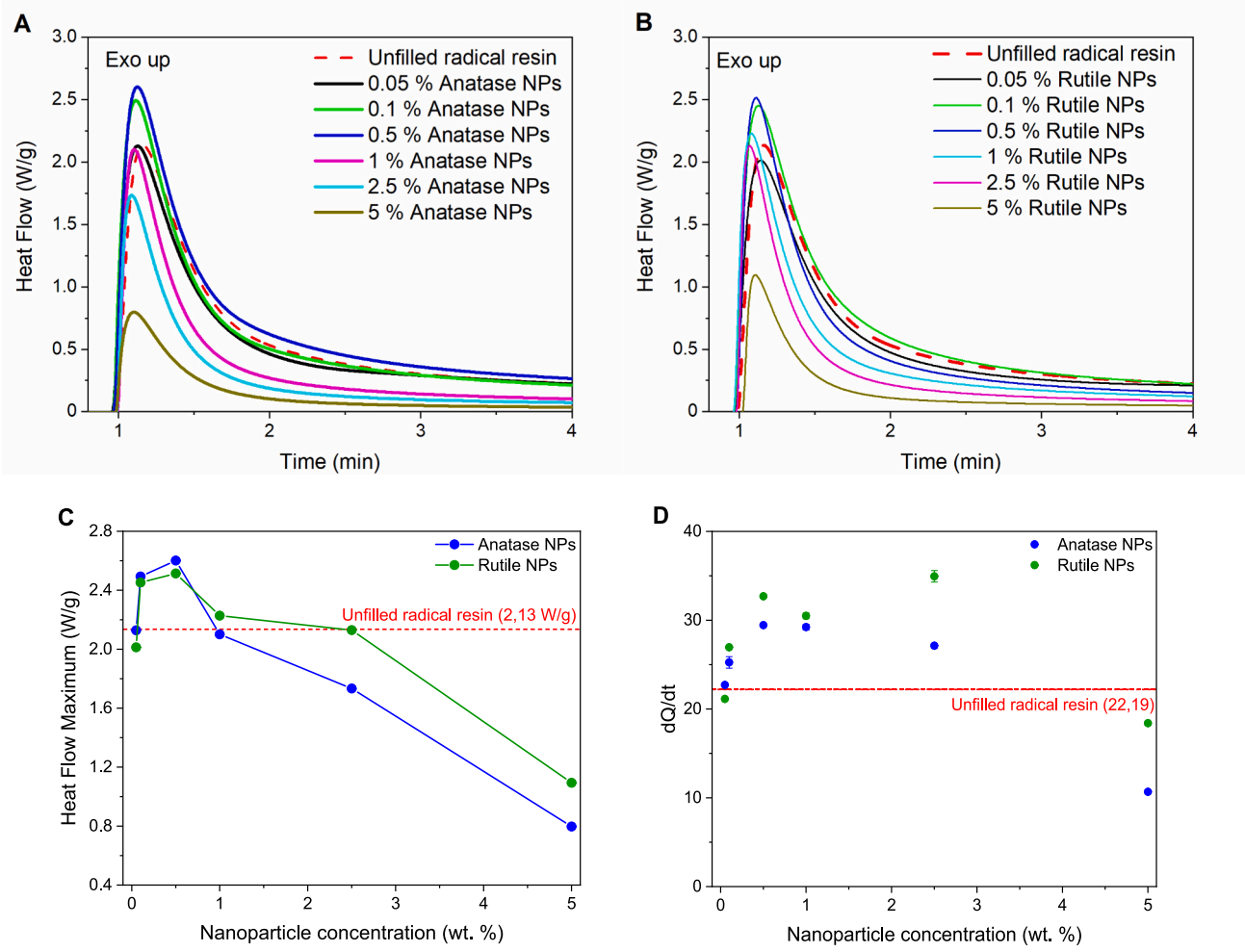

Fig. 6. Photo-DSC curves of radical resin reinforced with (A) anatase and (B) rutile nanoparticles, (C) maximum of exothermic peak formed during measurement, and (D) the heat flow rate (dQ/dt) as a function of nanoparticle concentration measured at 405 nm light wavelength.

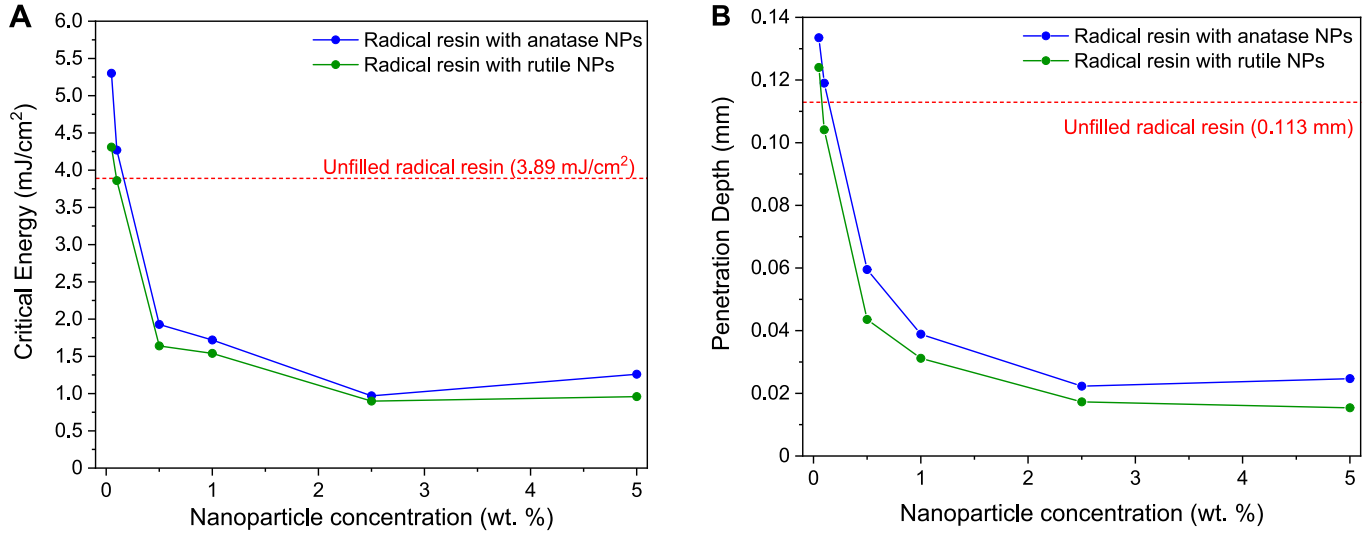

Fig. 7. (A) Critical energy, and (B) penetration depth as a function of nanoparticle concentration for radical resin mixtures containing anatase and rutile NPs cured at 405 nm.

the NP concentration in Fig. 8 and S18, respectively. Noteworthy, the cationic resin cured at the rate of 0.023 s^{-1} (Fig. 8B), nearly two times slower than the radical resin (0.043 s^{-1}, Fig. 5B) despite curing with higher intensity light. Analogical data for 365 nm curing are provided in Fig. S19–21.

Semiconducting metal oxide NPs do not act as a photoinitiator

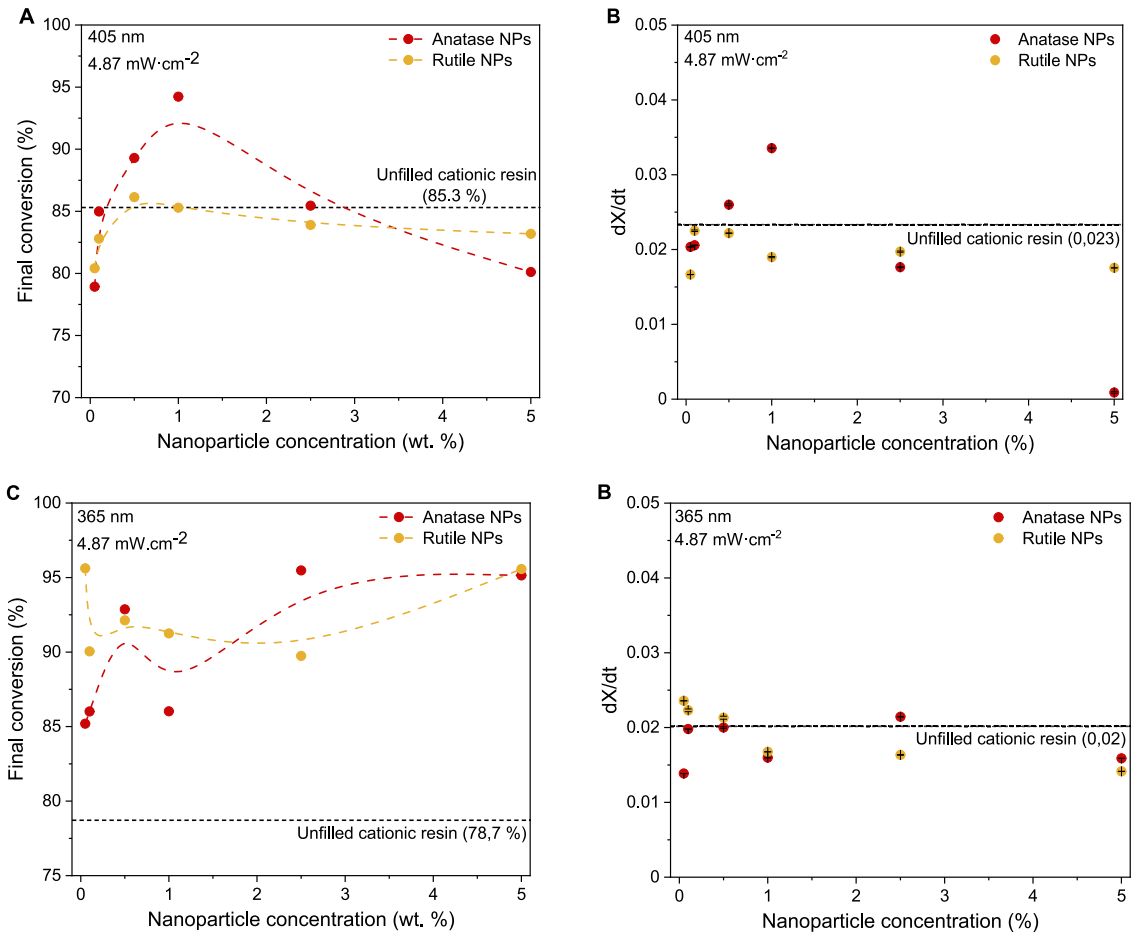

Fig. 8. Final conversion of the ECC epoxy group (A, C), the conversion rate (d*X*/d*t*) as a function of the nanoparticle concentration (B, D), measured at 405 nm (A, B) or 365 nm (C, D) with light intensity 4.87 mW·cm^{-2}. The dashed lines represent a guide for eyes. The standard deviation of final conversion (A, C) is very small, at 0.75 pp.

during the cationic polymerization, yet they can bring photosensitizing properties, as demonstrated by CV (Fig. 3). Using 405 nm wavelength LED light (Fig. 8A, B), anatase NPs increase the final conversions and d*X*/d*t* of the ECC epoxy groups, compared to the unfilled cationic resin. The effect culminates at 1 wt% while high NP loadings (>2.5 wt%) are no longer favorable for the reaction course. That correlates well with the CV measurement, in which anatase NPs enhance the electron-transfer, increasing the kinetics or reaction rate. Conversely to free-radical resin, rutile NPs bring no improvement to the final conversion and d*X*/d*t* (Fig. 8A, B) at 405 nm curing. Similar results with nearly no change in d*X*/d*t* is observed for both rutile and anatase at 365 nm curing (Fig. 8D). Despite NPs increasing the final conversions (Fig. 8C), it suggests that the photosensitizing capability of the semiconductive NPs to the cationic photopolymerization is driven by their electron-transfer properties. On the contrary, photoexcitation cancels the photosensitizing effect. Similar results were obtained when analyzing the conversion of the oxirane group of NGDE, shown in Fig. S17 and S20.

The photo-DSC curves of the pure cationic resin and its nanocomposite mixtures are shown in Fig. 9A, B. The maximum of endothermic peak and the rate of heat flow rate (d*Q*/d*t*) are provided in Fig. 9C, D, respectively. The cationic polymerization generates weaker heat flow with less pronounced maxima (Fig. 9A, B) than the free-radical resin (Fig. 6), corresponding to its slower curing rate. Accordingly, the reaction onset represented by d*Q*/d*t* rate is also slower (Fig. 9D).

The heat flow maxima revealed that anatase enhances the heat flow at low concentrations (< 1 wt%), while higher anatase concentration or rutile NPs reduced the detected heat flow (Fig. 9C). That, similar to real-time FTIR, points to the anatase's photosensitizing ability to the cationic resin. However, the detected heat flow consists not only of the reaction heat but also of electron-hole processes occurring on the NP surface in the case of the radical resin. Nevertheless, the presented results explain the puzzling discrepancy in the frontal polymerization (FP) in the presence of SiO_2 NPs (band gap ≈ 9 eV). FP is a special regime of polymerization propagating as front self-sustained by the reaction heat generated in the neighboring region. The front propagation rate is sensitive to the reaction heat evolution and any potential heat losses. Davtyan, et al. [55] reported no propagation rate variance for FP of free-radical acrylics up to NP content of 20 wt%. On the contrary, Lepcio, et al. [56] observed that 1 vol% of NPs (≈ 2.5 wt%) significantly slow down the propagation and even disrupt the frontal regime of cationic epoxy formulation in some cases. These findings correlate well with the currently presented results, concluding that the kinetical changes are tied to the specific reaction mechanism of the FP formulation.

The cationic resin was 3D printed with the laser SLA technology providing higher irradiance (15.67 mW·cm^{-2}) than the M-SLA equipped with LEDs used for the free-radical acrylic resin due to its slower photopolymerization. The E_c (Fig. 10A) and D_p (Fig. 10B) dependence on the NP concentration obtained from the Jacobs working curves (Fig. S22) further confirm its slower curing. While the cationic resin's E_c (404.7 mJ·cm^2) is roughly 100 times higher than that of the free-radical resin (3.89 mJ·cm^2), the D_p is even 190 times larger, taking the values of 21.5 and 0.113 mm for the cationic and free-radical resin, respectively.

In contrast to the free-radical mechanism, the incorporation of TiO_2 NPs into the cationic resin mostly increased E_c (Fig. 10A). As expected,

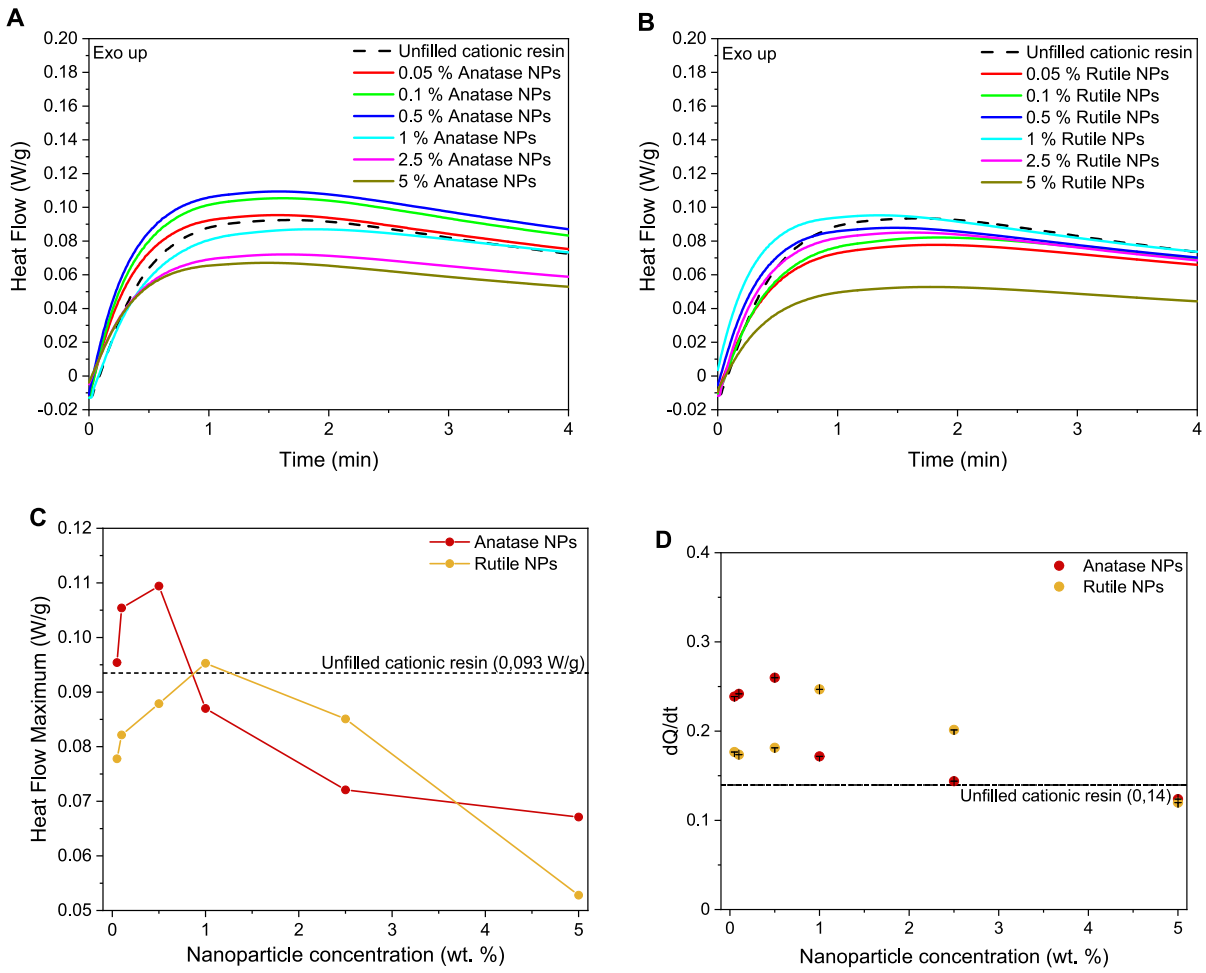

Fig. 9. Photo-DSC curves of cationic resin reinforced with (A) anatase and (B) rutile nanoparticles, (C) maximum of exothermic peak formed during measurement, and (D) the heat flow rate (dQ/dt) as a function of nanoparticle concentration measured 405 nm light wavelength.

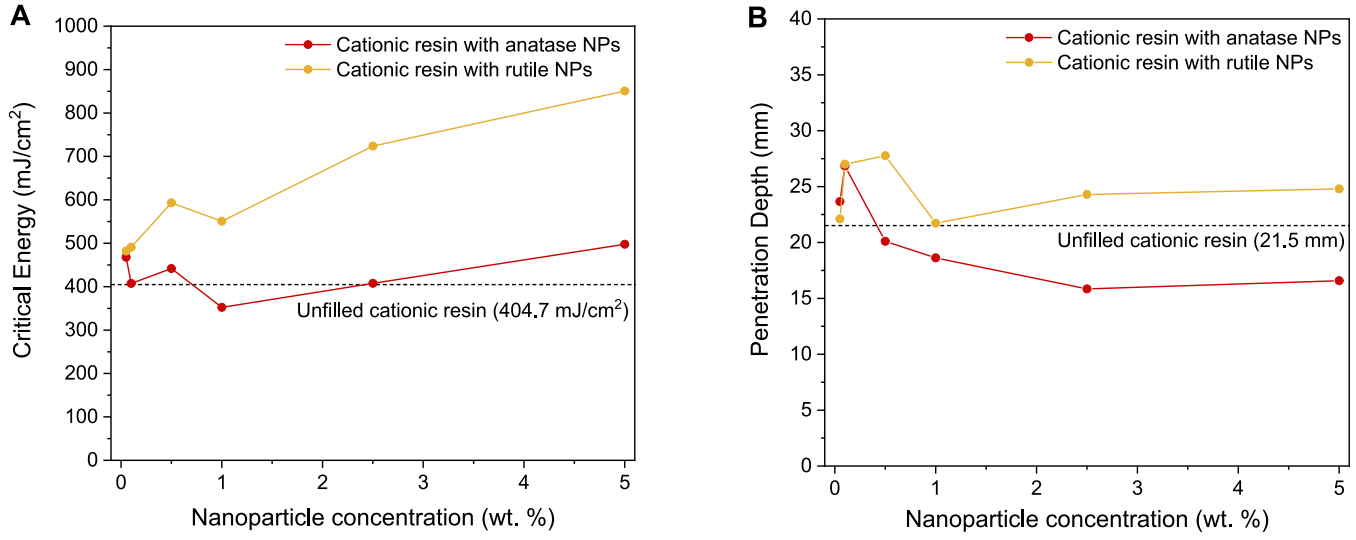

Fig. 10. (A) Critical energy and (B) penetration depth as a function of nanoparticle concentration for cationic resin filled with anatase and rutile cured at 405 nm.

anatase performed better than rutile, having a less pronounced adverse effect on the E_c. On the other hand, anatase NPs decreased D_p at all concentrations above 0.25 wt% unfilled cationic resin. However, the observed E_c and D_p values for anatase and rutile NPs correlate well with real-time FTIR and photo-DSC data. This also provides further evidence of the electron-transfer importance in the cationic polymerization photosensitizing by semiconductor metal oxide NPs.

4. Conclusions

This study investigated the incorporation of anatase and rutile polymorphs of TiO_2 NPs into a free-radical acrylic and cationic epoxy photopolymer 3D printing resin. The emphasis was placed on the different band gap energies of NPs, which lied below (rutile) and above (anatase) the photon energy at 405 nm, the wavelength used by common 3D printers. In addition, different processing parameters, e.g., the light wavelength, the light intensity, or the NP concentration, were tested to gain a complex understanding of the NP influence on the photocuring process. Our results suggest that both anatase and rutile are capable of photocatalytic effect, in which free charge carriers directly initiate the free-radical polymerization, yet the effectivity depends on the band gap energy, curing wavelength, light absorption efficiency and the electron transfer efficiency. At 405 nm, rutile increases the monomer conversion and reaction kinetics up to 1 wt%. However, anatase outperformed rutile at 365 nm as a consequence of a lower recombination rate.

On the other hand, the TiO_2 NPs interaction with the cationic photopolymerization followed a different mechanism. To the best of authors' knowledge, this has not been reported in any previous study. The NPs did not photoinitiate the reaction, but they acted as a photosensitizer. That means they absorbed light to form excited species, which then created an excited complex between the NP and the cationic photoinitiator, thereby facilitating the reaction initiation. A more pronounced photosensitizing was observed for anatase, while rutile improved the final conversion or curing rate only to a very limited extent.

Finally, we propose that cyclic voltammetry is an outstanding technique to analyze the electron transfer processes with semiconducting metal oxide NPs in photopolymerization reactions. This technique can better compare different mechanisms of the TiO_2 influence on the photoinitiation and distinguish between a photoinitiator and a photosensitizer. The acquired data may bring about additional progress in the preparation of polymer nanocomposites reinforced with semiconducting metal oxide NPs, which has the potential to facilitate the preparation of functional nanocomposite materials using vat 3D printing.

CRediT authorship contribution statement

Martina Korčušková: Writing – review & editing, Writing – original draft, Visualization, Investigation, Formal analysis, Data curation, Conceptualization. **Juraj Svatík:** Investigation, Formal analysis, Data curation. **Wiktoria Tomal:** Methodology, Investigation, Formal analysis, Data curation. **Aneta Šikyňová:** Formal analysis. **Vishakha Vishakha:** Investigation, Formal analysis. **Filip Petko:** Methodology, Investigation. **Mariusz Galek:** Resources, Methodology. **Paweł Stalmach:** Resources, Methodology. **Joanna Ortyl:** Writing – review & editing, Supervision, Conceptualization. **Petr Lepcio:** Writing – review & editing, Writing – original draft, Validation, Supervision, Resources, Project administration, Methodology, Investigation, Funding acquisition, Formal analysis, Data curation, Conceptualization.

Declaration of competing interest

The authors declare that they have no known competing financial interests or personal relationships that could have appeared to influence the work reported in this paper.

Data availability

The processed data required to reproduce these findings cannot be shared at this time due to technical or time limitations.

Acknowledgement

The authors express their gratitude to David Pavlinak and Andrej Vozárik (both Central European Institute of Technology, Brno University of Technology) for their help with optical experiments. The authors also gratefully acknowledge the GF21-43070L project supported by the GAČR (Czechia). Martina Korčušková and Juraj Svatík acknowledge the internal student grant CEITEC VUT-K-22-7719, which is realized within the project Quality Internal Grants of BUT (KInG BUT), Reg. No. CZ.02.2.69/0.0/0.0/19_073/0016948, financed from the OP RDE. The authors acknowledge the CzechNanoLab Research Infrastructure supported by MEYS CR (LM2023051) for providing equipment for optical and microscopical analysis.

Appendix A. Supplementary data

Supplementary data to this article can be found online at https://doi.org/10.1016/j.reactfunctpolym.2024.105923.

References

[1] A. Medellin, W. Du, G. Miao, J. Zou, Z. Pei, C. Ma, Vat photopolymerization 3D printing of nanocomposites: a literature review, J Micro Nanomanuf 7 (2019), https://doi.org/10.1115/1.4044288.
[2] J. Shan, Z. Yang, G. Chen, Y. Hu, Y. Luo, X. Dong, W. Zheng, W. Zhou, Design and synthesis of free-radical/cationic photosensitive resin applied for 3D printer with liquid crystal display (LCD) irradiation, Polymers (Basel) 12 (2020), https://doi.org/10.3390/POLYM12061346.
[3] I. Gibson, D. Rosen, B. Stucker, Additive Manufacturing Technologies, Springer New York, New York, NY, 2015, https://doi.org/10.1007/978-1-4939-2113-3.
[4] J.P. Fouassier, X. Allonas, D. Burget, Photopolymerization reactions under visible lights: principle, mechanisms and examples of applications, Prog. Org. Coat. 47 (2003) 16–36, https://doi.org/10.1016/S0300-9440(03)00011-0.
[5] B. Husár, M. Hatzenbichler, V. Mironov, R. Liska, J. Stampfl, A. Ovsianikov, Photopolymerization-based additive manufacturing for the development of 3D porous scaffolds, in: Biomaterials for Bone Regeneration, Elsevier, 2014, pp. 149–201, https://doi.org/10.1533/9780857098104.2.149.
[6] C. Mendes-Felipe, J. Oliveira, I. Etxebarria, J.L. Vilas-Vilela, S. Lanceros-Mendez, State-of-the-art and future challenges of UV curable polymer-based smart materials for printing technologies, Adv Mater Technol 4 (2019) 1800618, https://doi.org/10.1002/admt.201800618.
[7] M. Korčušková, V. Sevriugina, F. Ondreáš, J. Svatík, W. Tomal, V. Vishakha, J. Ortyl, P. Lepcio, Photoactivity, conversion kinetics, nanoreinforcement, post-curing, and electric/dielectric properties of functional 3D printable photopolymer resin filled with bare and alumina-doped ZnO nanoparticles, Polym. Test. 116 (2022) 107798, https://doi.org/10.1016/j.polymertesting.2022.107798.
[8] P. Lepcio, F. Ondreas, K. Zarybnicka, M. Zboncak, O. Caha, J. Jancar, Bulk polymer nanocomposites with preparation protocol governed nanostructure: the origin and properties of aggregates and polymer bound clusters, Soft Matter 14 (2018) 2094–2103, https://doi.org/10.1039/C8SM00150B.
[9] F. Ondreas, P. Lepcio, M. Zboncak, K. Zarybnicka, L.E. Govaert, J. Jancar, Effect of nanoparticle organization on molecular mobility and mechanical properties of polymer nanocomposites, Macromolecules 52 (2019) 6250–6259, https://doi.org/10.1021/acs.macromol.9b01197.
[10] R. Moriche, J. Artigas, L. Reigosa, M. Sánchez, S.G. Prolongo, A. Ureña, Modifications induced in photocuring of Bis- GMA/TEGDMA by the addition of graphene nanoplatelets for 3D printable electrically conductive nanocomposites, Compos. Sci. Technol. 184 (2019) 107876, https://doi.org/10.1016/j.compscitech.2019.107876.
[11] G. Wang, N.S. Hill, D. Zhu, P. Xiao, M.L. Coote, M.H. Stenzel, Efficient photoinitiating system based on diaminoanthraquinone for 3D printing of polymer/carbon nanotube nanocomposites under visible light, ACS Appl Polym Mater 1 (2019) 1129–1135, https://doi.org/10.1021/acsapm.9b00140.
[12] M.N. dos Santos, C.V. Opelt, F.H. Lafratta, C.M. Lepienski, S.H. Pezzin, L.A. F. Coelho, Thermal and mechanical properties of a nanocomposite of a photocurable epoxy-acrylate resin and multiwalled carbon nanotubes, Mater. Sci. Eng. A 528 (2011) 4318–4324, https://doi.org/10.1016/j.msea.2011.02.036.
[13] V. Sevriugina, D. Pavliňák, F. Ondreáš, O. Jašek, M. Štaffová, P. Lepcio, Matching low viscosity with enhanced conductivity in vat photopolymerization 3D printing: disparity in the electric and rheological percolation thresholds of carbon-based nanofillers is controlled by the matrix type and filler dispersion, ACS Omega 8 (2023) 45566–45577, https://doi.org/10.1021/acsomega.3c05683.
[14] J. Ma, Y. Lin, Y.-W. Kim, Y. Ko, J. Kim, K.H. Oh, J.-Y. Sun, C.B. Gorman, M. A. Voinov, A.I. Smirnov, J. Genzer, M.D. Dickey, Liquid metal nanoparticles as initiators for radical polymerization of vinyl monomers, ACS Macro Lett. 8 (2019) 1522–1527, https://doi.org/10.1021/acsmacrolett.9b00783.
[15] K.C. Anyaogu, X. Cai, D.C. Neckers, Gold nanoparticle photopolymerization of acrylates, Macromolecules 41 (2008) 9000–9003, https://doi.org/10.1021/ma801391p.
[16] S. Mubarak, D. Dhamodharan, N. Divakaran, M.B. Kale, T. Senthil, L. Wu, J. Wang, Enhanced mechanical and thermal properties of stereolithography 3d printed structures by the effects of incorporated controllably annealed anatase TiO2 nanoparticles, Nanomaterials 10 (2020), https://doi.org/10.3390/nano10010079.
[17] S. Dadashi-Silab, A.M. Asiri, S.B. Khan, K.A. Alamry, Y. Yagci, Semiconductor nanoparticles for photoinitiation of free radical polymerization in aqueous and

organic media, J. Polym. Sci. A Polym. Chem. 52 (2014) 1500–1507, https://doi.org/10.1002/pola.27145.
[18] S. Dadashi-Silab, Y. Yar, H. Yagci Acar, Y. Yagci, Magnetic iron oxide nanoparticles as long wavelength photoinitiators for free radical polymerization, Polym. Chem. 6 (2015) 1918–1922, https://doi.org/10.1039/C4PY01658K.
[19] C.S. Ng, A.S. Subramanian, P.C. Su, Zinc oxide nanoparticles as additives for improved dimensional accuracy in vat photopolymerization, Addit. Manuf. 59 (2022), https://doi.org/10.1016/j.addma.2022.103118.
[20] P. Riente, T. Noël, Application of metal oxide semiconductors in light-driven organic transformations, Catal Sci. Technol. 9 (2019) 5186–5232, https://doi.org/10.1039/C9CY01170F.
[21] K.B. Riad, A.A. Arnold, J.P. Claverie, S.V. Hoa, P.M. Wood-Adams, Photopolymerization using metal oxide semiconducting nanoparticles for epoxy-based coatings and patterned films, ACS Appl Nano Mater 3 (2020) 2875–2880, https://doi.org/10.1021/acsanm.0c00147.
[22] M. Sangermano, A. Priola, G. Kortaberria, A. Jimeno, I. Garcia, I. Mondragon, G. Rizza, Photopolymerization of epoxy coatings containing iron-oxide nanoparticles, Macromol. Mater. Eng. 292 (2007) 956–961, https://doi.org/10.1002/mame.200700093.
[23] S. Dadashi-Silab, S. Doran, Y. Yagci, Photoinduced electron transfer reactions for macromolecular syntheses, Chem. Rev. 116 (2016) 10212–10275, https://doi.org/10.1021/acs.chemrev.5b00586.
[24] X. Ren, W. Liu, Q. Yao, S. Wang, W. Liu, H. Gu, D. Wang, J. Fan, X. Peng, A UV-LED excited photoinitiator with low toxicity and low migration for photocurable inks, Dyes Pigments 200 (2022) 110133, https://doi.org/10.1016/j.dyepig.2022.110133.
[25] M. Popal, J. Volk, G. Leyhausen, W. Geurtsen, Cytotoxic and genotoxic potential of the type I photoinitiators BAPO and TPO on human oral keratinocytes and V79 fibroblasts, Dent. Mater. 34 (2018) 1783–1796, https://doi.org/10.1016/j.dental.2018.09.015.
[26] H. Zhou, Y. Huang, Y. Zhang, D. Song, H. Huang, C. Zhong, G. Ye, Hydrogen abstraction of carbon/phosphorus-containing radicals in photoassisted polymerization, RSC Adv. 6 (2016) 68952–68959, https://doi.org/10.1039/c6ra00156d.
[27] J. Lalevée, J.-P. Fouassier (Eds.), Photopolymerisation Initiating Systems, The Royal Society of Chemistry, 2018, https://doi.org/10.1039/9781788013307.
[28] J. Kabatc, J. Ortyl, K. Kostrzewska, New kinetic and mechanistic aspects of photosensitization of iodonium salts in photopolymerization of acrylates, RSC Adv. 7 (2017) 41619–41629, https://doi.org/10.1039/c7ra05978g.
[29] S. Glass, B. Trinklein, B. Abel, A. Schulze, TiO2 as photosensitizer and photoinitiator for synthesis of photoactive TiO2-PEGDA hydrogel without organic photoinitiator, Front. Chem. 6 (2018), https://doi.org/10.3389/fchem.2018.00340.
[30] S. Peiris, H.B. de Silva, K.N. Ranasinghe, S.V. Bandara, I.R. Perera, Recent development and future prospects of TiO2 photocatalysis, J. Chin. Chem. Soc. 68 (2021) 738–769, https://doi.org/10.1002/jccs.202000465.
[31] M.C. Mathpal, A.K. Tripathi, M.K. Singh, S.P. Gairola, S.N. Pandey, A. Agarwal, Effect of annealing temperature on Raman spectra of TiO2 nanoparticles, Chem. Phys. Lett. 555 (2013) 182–186, https://doi.org/10.1016/j.cplett.2012.10.082.
[32] M.R. Al-Mamun, S. Kader, M.S. Islam, M.Z.H. Khan, Photocatalytic activity improvement and application of UV-TiO2 photocatalysis in textile wastewater treatment: a review, J. Environ. Chem. Eng. 7 (2019), https://doi.org/10.1016/j.jece.2019.103248.
[33] X. Zhao, G. Zhang, Z. Zhang, TiO2-based catalysts for photocatalytic reduction of aqueous oxyanions: state-of-the-art and future prospects, Environ. Int. 136 (2020), https://doi.org/10.1016/j.envint.2019.105453.
[34] S. Mubarak, D. Dhamodharan, M.B. Kale, N. Divakaran, T. Senthil, S.P.L. Wu, J. Wang, A novel approach to enhance mechanical and thermal properties of SLA 3D printed structure by incorporation of metal–metal oxide nanoparticles, Nanomaterials 10 (2020) 217, https://doi.org/10.3390/nano10020217.
[35] S. Ghosh, A.P. Das, Modified titanium oxide (TiO2) nanocomposites and its array of applications: a review, Toxicol. Environ. Chem. 97 (2015) 491–514, https://doi.org/10.1080/02772248.2015.1052204.
[36] J. He, Y. En Du, Y. Bai, J. An, X. Cai, Y. Chen, P. Wang, X. Yang, Q. Feng, Facile formation of anatase/rutile TiO2 nanocomposites with enhanced photocatalytic activity, Molecules 24 (2019), https://doi.org/10.3390/molecules24162996.
[37] A. Nicosia, F. Vento, G.M. di Mari, L. D'urso, P.G. Mineo, TiO2-based nanocomposites thin film having boosted photocatalytic activity for xenobiotics water pollution remediation, Nanomaterials 11 (2021) 1–11, https://doi.org/10.3390/nano11020400.
[38] W. Tomal, J. Ortyl, Influence of a non-reactive additive on the photocuring and 3D-VAT printing processes of PEGDA: complementary studies, Eur. Polym. J. 180 (2022), https://doi.org/10.1016/j.eurpolymj.2022.111588.
[39] H. Nawaz, M. Umar, R. Maryam, I. Nawaz, H. Razzaq, T. Malik, X. Liu, Polymer nanocomposites based on TiO $_2$ as a reinforcing agent: an overview, Adv. Eng. Mater. 24 (2022) 2200844, https://doi.org/10.1002/adem.202200844.
[40] W. Liao, X. Ni, Y. Zhou, Cationic and free radical polymerization initiated by a visible-light sensitive complex based on the photocatalytic decarboxylation of carboxylic acid, J. Catal. 361 (2018) 423–430, https://doi.org/10.1016/j.jcat.2018.03.005.
[41] H. Hajizadeh, S.J. Peighambardoust, S.H. Peighambardoust, D. Peressini, Physical, mechanical, and antibacterial characteristics of bio-nanocomposite films loaded with ag-modified SiO2 and TiO2 nanoparticles, J. Food Sci. 85 (2020) 1193–1202, https://doi.org/10.1111/1750-3841.15079.
[42] X. Liu, H. Sun, S. Liu, Y. Jiang, B. Yu, N. Ning, M. Tian, L. Zhang, Mechanical, dielectric and actuated properties of carboxyl grafted silicone elastomer composites containing epoxy-functionalized TiO2 filler, Chem. Eng. J. 393 (2020), https://doi.org/10.1016/j.cej.2020.124791.
[43] W. Tomal, D. Krok, A. Chachaj-Brekiesz, P. Lepcio, J. Ortyl, Harnessing light to create functional, three-dimensional polymeric materials: multitasking initiation systems as the critical key to success, Addit. Manuf. 48 (2021), https://doi.org/10.1016/j.addma.2021.102447.
[44] J. Ortyl, M. Galek, F. Petko, K. Machowski, N. Szmaciarz, New iodonium salts, a method of preparation of new iodonium salts, application of new iodonium salts, new thiophene derivatives, methods of preparation of thiophene derivatives and application of thiophene derivatives, P.429353, 2019.
[45] P. Makuła, M. Pacia, W. Macyk, How to correctly determine the band gap energy of modified semiconductor photocatalysts based on UV-vis spectra, J. Phys. Chem. Lett. 9 (2018) 6814–6817, https://doi.org/10.1021/acs.jpclett.8b02892.
[46] O. Frank, M. Zukalova, B. Laskova, J. Kürti, J. Koltai, L. Kavan, Raman spectra of titanium dioxide (anatase, rutile) with identified oxygen isotopes (16, 17, 18), Phys. Chem. Chem. Phys. 14 (2012) 14567–14572, https://doi.org/10.1039/c2cp42763j.
[47] S. Challagulla, K. Tarafder, R. Ganesan, S. Roy, Structure sensitive photocatalytic reduction of nitroarenes over TiO2, Sci. Rep. 7 (2017), https://doi.org/10.1038/s41598-017-08599-2.
[48] N. Elgrishi, K.J. Rountree, B.D. McCarthy, E.S. Rountree, T.T. Eisenhart, J. L. Dempsey, A practical beginner's guide to cyclic voltammetry, J. Chem. Educ. 95 (2018) 197–206, https://doi.org/10.1021/acs.jchemed.7b00361.
[49] W. Wang, X. Fan, J. Liu, C. Yan, C. Zeng, Temperature-related reaction kinetics of the vanadium(iv)/(v) redox couple in acidic solutions, RSC Adv. 4 (2014) 32405–32411, https://doi.org/10.1039/C4RA04278F.
[50] P. Lepcio, F. Ondreáš, K. Zárybnická, M. Zbončák, J. Svatík, J. Jančář, Phase diagram of bare particles in polymer nanocomposites: uniting solution and melt blending, Polymer (Guildf) 230 (2021) 124033, https://doi.org/10.1016/j.polymer.2021.124033.
[51] E. Andrzejewska, Photopolymerization kinetics of multifunctional monomers, 2001, https://doi.org/10.1016/S0079-6700(01)00004-1.
[52] M. Štaffová, F. Ondreáš, J. Svatík, M. Zbončák, J. Jančář, P. Lepcio, 3D printing and post-curing optimization of photopolymerized structures: basic concepts and effective tools for improved thermomechanical properties, Polym. Test. 108 (2022) 107499, https://doi.org/10.1016/j.polymertesting.2022.107499.
[53] Q. Guo, C. Zhou, Z. Ma, X. Yang, Fundamentals of TiO2 photocatalysis: concepts, mechanisms, and challenges, Adv. Mater. 31 (2019), https://doi.org/10.1002/adma.201901997.
[54] R. Qian, H. Zong, J. Schneider, G. Zhou, T. Zhao, Y. Li, J. Yang, D.W. Bahnemann, J.H. Pan, Charge carrier trapping, recombination and transfer during TiO2 photocatalysis: an overview, Catal. Today 335 (2019) 78–90, https://doi.org/10.1016/j.cattod.2018.10.053.
[55] S.P. Davtyan, A.A. Berlin, K. Shik, A.O. Tonoyan, S.Z. Rogovina, Polymer nanocomposites with a uniform distribution of nanoparticles in a polymer matrix synthesized by the frontal polymerization technique, Nanotechnol Russ 4 (2009) 489–498, https://doi.org/10.1134/S1995078009070106.
[56] P. Lepcio, J. Daguerre-Bradford, A.M. Cristadoro, M. Schuette, A.J. Lesser, Frontally polymerized foams: thermodynamic and kinetical aspects of front hindrance by particles, Mater. Horiz. 10 (2023) 2989–2996, https://doi.org/10.1039/D2MH01553F.